LOW-FREQUENCY DYNAMIC RESPONSE OF FLOATING OFFSHORE WIND FARMS WITH SHARED MOORING SYSTEMS

Rajendran Arun Ingersol[1,2,3], Yanlin Shao[3], Zhilong Wei[3,*]

[1]Technology Centre for Offshore and Marine, Singapore (TCOMS)
[2]National University of Singapore, Singapore
[3]Technical University of Denmark, Kgs. Lyngby, Denmark

ABSTRACT

Shared mooring systems are a promising pathway to reduce capital and footprint costs for floating offshore wind farms (FOWFs). This work investigates the low-frequency (LF) surge-sway responses of multi-turbine arrays with shared moorings versus individually moored turbines. This study examines a single-turbine baseline and a 2×2 lattice with shared mooring lines using both frequency- and time-domain analyses. In the frequency domain, mechanical coupling through shared mooring lines is reflected in the cross-coupling coefficients in the restoring matrix. In parallel, time-domain simulations in SIMA (SIMO-RIFLEX) of the same configurations are performed to obtain response statistics and power spectral densities (PSDs) for cross-validation. Modal and nodal analyses reveal that shared mooring introduces distinct array modes and multiple LF PSD peaks, whereas the individual-mooring baseline exhibits a single, narrow-band peak near its natural frequency. The in-line modal shapes are found to be associated with higher response and excitation loads. Causes of potential failure potential failure of shared line or anchor line are also identified from the mode shapes. Time-domain simulations corroborate frequency-domain predictions, confirming multiple LF peaks at eigenfrequencies identified by modal analysis and a single dominant peak for the individual system. These results show that the shared system's dynamic response differs significantly from the individual mooring system highlights the need for a more robust design consideration for shared mooring systems of FOWFs.

Keywords: shared moorings, floating offshore wind farms (FOWFs), slow-drift response, modal analysis

1. INTRODUCTION

Shared mooring is an innovative design concept aimed at reducing the construction costs of floating offshore wind farms (FOWFs). This system minimizes the number of mooring lines and anchors required by either sharing anchors or connecting structures to adjacent ones. This approach decreases both installation costs and material usage [1]. However, shared mooring lines introduce coupling between floating offshore wind turbines (FOWTs), adding complexity to the system's dynamics relative to individually moored turbines, especially in the low-frequency (slow-drift) range, where horizontal-motion resonance can occur.

Various studies have examined shared mooring systems. These include static, frequency-domain, and time-domain analyses.

A static analysis was conducted in [2] on a dual spar (the NREL 5MW wind turbine on the OC3 spar floating system) with shared mooring systems, in which different mooring properties were investigated. Irvine's method [3] was used to model the shared mooring line by using static positions obtained from static analysis in SIMA [4]. Their results showed that the shared mooring lines significantly affect the restoring force when there is an offset to the FOWT.

In [5], a quasi-static analysis was performed on a pilot-scale floating wind farm using the NREL 5MW offshore reference wind turbine. Both frequency and time-domain analyses were conducted on various mooring configurations of 4 FOWTs in a $2\times$ 2 square array as shown in their Fig. 1, and compared to a baseline single FOWT set-up. The results show that a wind direction of 45° represents the worst case with maximum displacement and line tension. They also show that significant cost savings are possible at water depths 400 m and above. At these depths, the cost of individual mooring lines attached to the seabed is much more than that of shared lines. However, slow-drift forces have been neglected in this study which may have a significant impact.

A shared mooring analysis using HAWC2Farm [6] was carried out for two 15 MW floating wind turbines on spar floaters with both shared mooring lines and shared anchors [7]. Their results concluded that the natural frequencies for the shared mooring line design with heavy chain mooring can be designed to be similar to the single FOWT by reducing the length of the shared line. However, since it is in shallower waters (200 m), even at tight lengths where the mooring forces are already significantly higher than the single FOWT, the shared lines tend to touch the seabed. For the shared anchor design with polyester mooring lines, where wind and wave loads were simulated, the loading on the upstream mooring line was 30% higher than the single

*Corresponding author: zhilwei@dtu.dk

FOWT counterpart and also twice as much surge motion as both the downstream FOWT and an individual FOWT.

A dynamic time-domain analysis of a row arrangement of FOWT farms was performed in [8]. Their results showed that increasing the number of coupled FOWTs by shared mooring lines increases the horizontal displacement. Moreover, the first mooring line in the force direction transfers the largest force to its anchor while the last FOWT in the chain moves relatively close to its anchor.

Among the studies, a noticeable gap remains between the findings from different research groups using frequency-domain [9] and time-domain approaches [10, 11]. The former reported substantial differences in dynamic response relative to individually moored systems, whereas the latter found no significant differences.

In [9], a frequency-domain analysis taking into account the second-order difference-frequency excitation wave loads was performed for a 2×2 lattice of four INO WINDMOOR 12 MW turbines [12]. A 1.5 MN proxy wind load at 45° was applied to each FOWT. Eigenmodes and eigenfrequencies were obtained from the coupled motion equations, with linear mooring stiffnesses extracted via a nonlinear static analysis. The results showed resonance in modal responses at difference frequencies coincident with the modal eigenfrequencies, and modal load spectra indicated loading across all frequencies.

A 10-FOWT farm layout is optimized in [10, 11] using quasi-static and dynamic analyses. Time-domain simulations (OpenFAST [13] for wind/wave kinematics, FAST.Farm [14] for array-level motions, and MoorDyn [15] for moorings) assessed station-keeping under different load cases, wind/wave headings, and three possible mooring system failure points. Despite added complexity from shared moorings, the selected staggered layout did not introduce any additional natural frequencies in surge or sway compared to the baseline of an individual FOWT.

This paper seeks to reconcile these viewpoints and tests whether the low-frequency dynamics of shared-mooring FOWTs differ from those of individually moored systems by applying both frequency- and time-domain analyses to the shared-mooring configuration proposed in [16], using the DTU 10 MW Reference Wind Turbine [17] on a spar buoy floater.

This paper is structured as follows. Section 2 defines the 2×2 lattice configuration of four FOWTs with shared mooring system. Section 3 details the methodology, including frequency-domain analysis, modal analysis, and time-domain simulation. Section 4 presents the results from each method. Finally, conclusions are drawn in Section 5.

2. MOORING SYSTEM MODEL

Fig. 1 shows a schematic of the spar buoy floater used in this study. The model parameters are reported in [10] and summarized here in Table 1. The fairlead points are placed at the outer radius (7.375 m) of the spar buoy as shown by the green diamond markers in Fig. 1.

Fig. 2 and Fig. 3 present schematics (not to scale) of the individual FOWT setup and the four FOWT setup with shared mooring systems, respectively. The 2×2 lattice configuration follows [9], whereas the parameters, such as FOWT position,

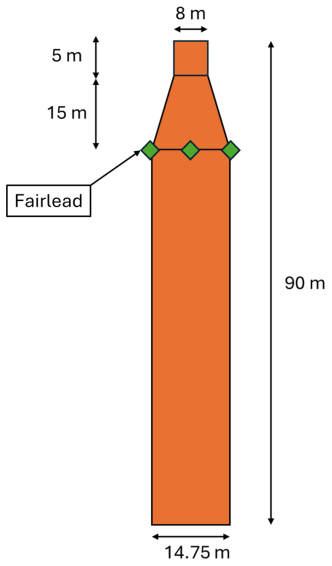

Parameter	Value
Draft	90 m
Fairlead depth	20 m
Base diameter	14.75 m
Top diameter (water surface level)	8 m
Centre of mass depth	78.2 m
Total displace volume	13781 m^3
Total mass (without ballasting)	1.251×10^7 kg

FIGURE 1: Spar buoy geometry (not to scale) and properties.

TABLE 1: Mooring line properties.

Property	Result
Diameter, d [m]	0.213
Mass Density [kg/m]	36.2
EA [MN]	49.45
MBL [MN]	7.735
Horizontal Length Shared Line [m]	1600
Horizontal Length Anchor Line [m]	1600
Unstretched Length Shared Line [m]	1545.1
Unstretched Length Anchor Line [m]	1640.1
Pre-Tension Shared Line [MN]	1.84
Pre-Tension Anchor Line [MN]	1.98

shared lines, and anchor lines, follow [10]. In both panels, "An" denotes anchor lines and "sl" denotes shared lines. Both the taut anchor lines and shared lines have a horizontal projected length of 1600 m. Anchors are installed on the seabed at a water depth of 600 m.

The design of the mooring lines follows the report on shared mooring published by NREL [10]. Accordingly, the present study employs a taut mooring system utilizing polyester mooring lines for both the anchor and shared lines. Linear restoring coefficients due to the mooring lines are obtained using MoorPy [18] with property relations taken from OrcaFlex [19]. A quadratic Maximum Breaking Load (MBL) equation was additionally modified and included by NREL, i.e., $\text{MBL}[\text{MN}] = 170490 \times d^2 \times 10^3$, where d is the rope diameter in meters. The resulting line properties are listed in Table 1.

3. METHODOLOGY

3.1. Frequency-Domain Analysis

In accordance with the model setup, only surge and sway for four FOWTs ($N_{\text{body}} = 4$) mechanically coupled through shared mooring lines are considered. Hydrodynamic coupling is as-

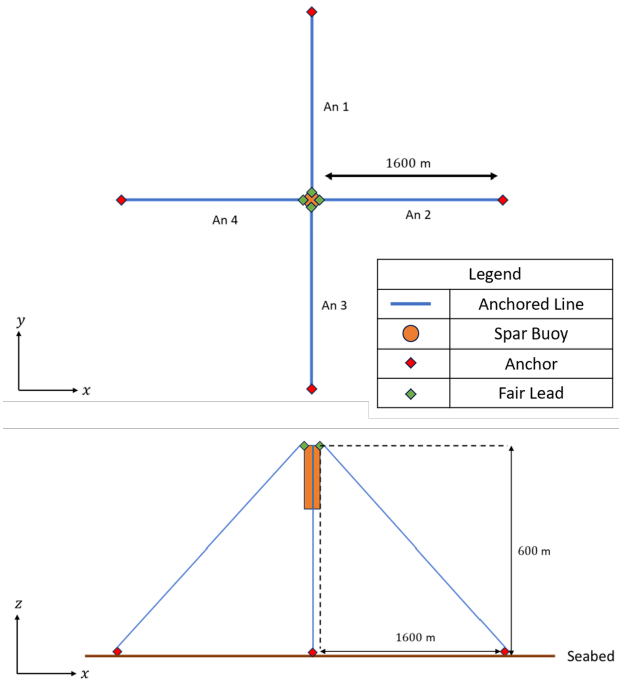

FIGURE 2: Top and side views of the individual FOWT.

sumed weak due to the required large distance between the turbines to ensure energy conversion efficiency and is neglected. The system therefore has $N_{\text{DOF}} = 2N_{\text{body}} = 8$ degrees of freedom (DOF). The following methodology extends straightforwardly to arbitrary N_{body} and all six DOFs per body.

The coupled equations of motion are similar to those for a single 6-DOF floater, but with extended dimensions:

$$\left[-\mu^2(\mathbf{M}+\mathbf{A}) + \mathrm{i}\mu\mathbf{B} + \mathbf{C}\right]\boldsymbol{\xi} = \mathbf{F}. \tag{1}$$

where $\mu > 0$ is the difference frequency and $\mathbf{M}, \mathbf{A}, \mathbf{B}, \mathbf{C} \in \mathbb{R}^{N_{\text{DOF}} \times N_{\text{DOF}}}$ are the coupled inertia, added mass, damping, and restoring matrices. In principle, the added mass matrix $\mathbf{A}$ is dependent on the difference-frequency μ. However, since the characteristic natural periods of surge and sway motions of the coupled system are more than 100 seconds, $\mathbf{A}(\mu)$ can be approximated by its zero-frequency asymptotics $\mathbf{A}(\mu = 0)$. At such low frequencies, the damping contribution from linear wave radiation to the damping matrix $\mathbf{B}$ is practically zero. Instead, the viscous drag on hull and mooring lines, as well as wave-drift damping, are relatively more important. The complex amplitudes of the second-order difference-frequency response and excitation are denoted by $\boldsymbol{\xi}$ and $\mathbf{F}$, respectively.

Let's define the inverse of the matrix on the left-hand side of Eq. (1) as

$$\mathbf{T} = \left[-\mu^2(\mathbf{M}+\mathbf{A}) + \mathrm{i}\mu\mathbf{B} + \mathbf{C}\right]^{-1}. \tag{2}$$

Using Einstein's notation, the response amplitude is

$$\xi_i = T_{ij} F_j, \quad i, j = 1, 2, \ldots, N_{\text{DOF}}. \tag{3}$$

As for a single floater, the power spectral density (PSD) of the excitation load F_j can be obtained following a similar procedure

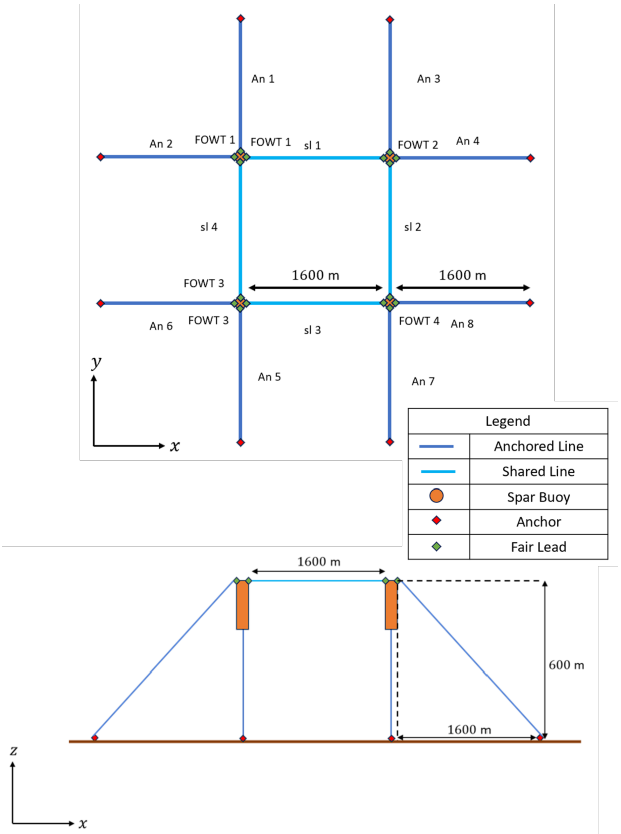

FIGURE 3: Top and side views of the 2×2 FOWTs with shared moorings.

for a single floater:

$$S_{F_j}(\mu) = 8\int_0^\infty S(\omega)S(\omega+\mu)\left|Q^j(\omega, \omega+\mu)\right|^2 \mathrm{d}\omega, \tag{4}$$

where $S(\omega)$ is the wave spectrum (JONSWAP here) and Q^j is the difference-frequency excitation quadratic transfer function (QTF) for the jth DOF, including phase shifts from the body's position relative to the QTF reference.

Similarly, the slow-drift response PSD in Einstein's notation is then

$$S_{\xi_i}(\mu) = \left|T_{ij}\right|^2 S_{F_j}(\mu), \quad i, j = 1, 2, \ldots, N_{\text{DOF}}. \tag{5}$$

As reported in [16], the total mass of one spar buoy is $m = 1.25 \times 10^7$ kg. The surge and sway added mass estimated via strip theory is 1.57×10^7 kg. This value is higher than that predicted by HydroD [20] in long waves, resulting in roughly 7% difference in total inertia. Because the spar buoys are axisymmetric, and that they are well-separated from each other with negligible hydrodynamic interactions, the resulting $\mathbf{A}$ and $\mathbf{M}$ are diagonal matrices.

The restoring matrix $\mathbf{C}$ was computed with MoorPy, a quasi-static mooring solver. A steady wind force of 1.5 MN at 45° is applied to each FOWT to let the floaters reach their horizontal equilibrium positions under operation conditions, thereby yielding a more realistic estimate of $\mathbf{C}$. The magnitude of the wind load is estimated from [10]. The spar buoy was modeled using the properties reported in [10] with an initial mass

$m = 1.25 \times 10^7$ kg, center of mass depth 78.2 m, and a water-plane area $A_{\mathrm{wp}} = 50.27\,\mathrm{m}^2$. Mooring-line properties are listed in Table 1. Mechanical coupling through shared mooring lines appears in the nonzero cross-coupling restoring coefficients in $\mathbf{C}$, which exhibits a bisymmetric structure (symmetric about both the main and anti-diagonals).

In the present frequency-domain analysis, only viscous drag is treated as a contribution to the damping matrix $\mathbf{B}$. Wave-drift damping is neglected here but it can be precomputed and included. Because the spar is axisymmetric about its vertical axis, the resulting hydrodynamic and viscous damping in surge and sway are directionally identical with negligible cross-terms. Combined with the dominance of spar buoy drag over mooring-line drag, the damping matrix $\mathbf{B}$ therefore reduces to a diagonal matrix. Using stochastic linearization of quadratic drag [21], the equivalent damping coefficient for the ith DOF is

$$B_{ii} = \frac{1}{2}\rho C_d A_p \sigma_{u_i} \sqrt{\frac{8}{\pi}}, \tag{6}$$

where C_d is the drag coefficient, A_p is the projected area in the flow direction, and σ_{u_i} is the standard deviation of the structure velocity of slow drift motion, given by the square root of the zeroth spectral moment of the velocity PSD:

$$\sigma_{u_i} = \sqrt{\int_0^\infty \left|\mathrm{i}\mu T_{ij}\right|^2 S_{F_j}(\mu)\mathrm{d}\mu}, \quad i, j = 1, 2, \ldots, N_{\mathrm{DOF}}. \tag{7}$$

In general, B_{ii} should be obtained iteratively until convergence is achieved. For a given value of C_d, the specific steps to find B_{ii} are as follows.

1. Begin with C_d, $S(\omega)$, $Q^j(\omega, \mu)$, and an initial guess of σ_{u_i}.
2. Apply the stochastic linearization (6) and compute B_{ii}.
3. Compute the matrix $\boldsymbol{T}$ using Eq. (2).
4. Compute the standard deviation of the structure velocity using Eq. (7).
5. Go back to Step 2 until convergence of σ_{u_i} and B_{ii} is achieved.

The iteration above is performed for a given drag coefficient C_d, which is influenced by several factors, such as Reynolds number Re, Keulegan-Carpenter number KC, and surface roughness Δ. Both Re and KC depend on the floater velocity, which is not known *a priori*.

To reduce the uncertainty of the selection of C_d, an empirical method suggested by DNV-RP-C205 [22] is used here to estimate C_d based on KC number. The empirical drag coefficient can be expressed as a function of KC number for both smooth and rough circular cylinders. At supercritical Reynolds numbers, C_d can be approximated by

$$C_d = C_{DS}(\Delta) \cdot \Psi(\mathrm{KC}). \tag{8}$$

Here the spar buoy is assumed to be smooth and constant $C_{DS} = 0.65$ is used. Given the spar buoy dimensions, the expression for

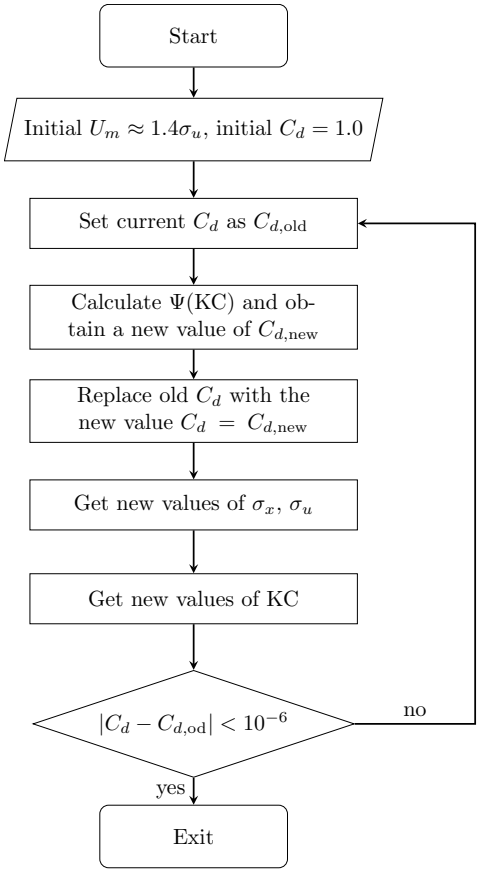

FIGURE 4: Flow chart to find the drag coefficient C_d based on KC number.

Ψ(KC) with KC < 12 is used here:

$$\Psi(\mathrm{KC}) = \begin{cases} C_\pi + 0.10(\mathrm{KC} - 12), & 2 \le \mathrm{KC} < 12, \\ C_\pi - 1.00, & 0.75 \le \mathrm{KC} < 2, \\ C_\pi - 1.00 - 2.00(\mathrm{KC} - 0.75), & \mathrm{KC} \le 0.75 \end{cases}, \tag{9}$$

where $C_\pi = 1.30$ for a smooth cylinder. The equation for KC is

$$\mathrm{KC} = \frac{U_m T}{D}, \tag{10}$$

where U_m denotes the wave orbital velocity, T the wave period, and D the diameter of the spar buoy. The above definition of KC is directly applicable to sinusoidal flow velocities due to, for instance, regular waves. In irregular waves, the flow-velocity amplitude is approximated as $U_m = \sqrt{2}\sigma_u \approx 1.4\sigma_u$.

Since C_d is a function of KC and thus the motion σ_u, an additional (outer) iteration is introduced to update C_d. This outer loop uses the iteration described above (for a prescribed C_d) as its inner loop. The whole workflow is illustrated in Fig. 4. In the flowchart, the block "Get new values of σ_x, σ_u" corresponds to the five-step iteration defined above. Although this method reduces the uncertainty in the selection of C_d, it is still a rough estimate. A more accurate C_d requires dedicated physical experiments.

The difference-frequency excitation QTFs, i.e., Q^j in Eq. (4), were computed with HydroD/WADAM [23] for a single spar buoy

over wave frequencies 0 rad/s to 3.35 rad/s with a wave heading of 45°. Because the spar buoy is axisymmetric, the surge and sway direction can be resolved simply by multiplying the QTF by $\cos\beta$ or $\sin\beta$, respectively. Here $\beta = 45°$ is the wave heading angle in the present study. Fig. 5 shows the real and imaginary parts of the QTF for all combinations of ω_i and ω_j.

Computing the full QTF requires solving the complete second-order boundary-value problem and, for slowly varying loads, evaluating interactions across all frequency pairs (ω_i, ω_j), which is computationally demanding. To reduce the cost, Newman's approximation is also considered in the present work:

$$Q^c_{ij} \approx \frac{1}{2}(Q^c_{ii} + Q^c_{jj}), \quad Q^s_{ij} \approx 0, \tag{11}$$

where Q^c_{ij} and Q^s_{ij} are the cosine and sine components of the QTF, respectively (alternatively, the real part and the opposite of the imaginary part). Comparison of the results using full QTF and Newman's approximation will be presented in a later section.

3.2. Modal Analysis

Modal analysis is a technique used to study dynamic characteristics, such as eigenmodes, and natural frequencies, by decomposing the response into a series of vibration modes known as modal shapes. Each mode represents a pattern of motion at a specific natural frequency.

A free-vibration problem without damping can be expressed by setting $\mathbf{B} = \mathbf{0}$ and $\mathbf{F} = \mathbf{0}$ in Eq.(1), which gives

$$-(\mathbf{M} + \mathbf{A})\omega^2 + \mathbf{C} = \mathbf{0}, \tag{12}$$

in which ω denotes the vibration frequencies following conventions. This is the generalized eigenvalue problem

$$\det\Big([-(\mathbf{M} + \mathbf{A})\omega^2 + \mathbf{C}]\Big) = 0, \tag{13}$$

$$[-(\mathbf{M} + \mathbf{A})\omega^2 + \mathbf{C}]\mathbf{v} = \mathbf{0}, \tag{14}$$

whose solutions yield N_{dof} natural frequencies ω and N_{dof} eigenvectors (mode shapes) $\mathbf{v}$ of the system. This modal analysis provides a first interpretation of the shared-mooring coupling, while the full low-frequency response further depends on hydrodynamic excitation and damping.

Let $\mathbf{\Phi} = [\mathbf{v_1}, \mathbf{v_2}, \ldots, \mathbf{v}_{\mathbf{N}_{\text{dof}}}] \in \mathbb{R}^{N_{\text{DOF}} \times N_{\text{DOF}}}$ collect the eigenvectors as columns. The modal load $\overline{\mathbf{F}}$ and modal response $\overline{\boldsymbol{\xi}}$ are given by

$$\mathbf{F} = \mathbf{\Phi}\overline{\mathbf{F}}, \quad \boldsymbol{\xi} = \mathbf{\Phi}\overline{\boldsymbol{\xi}}. \tag{15}$$

Premultiplying Eq. (1) by $\mathbf{\Phi}^\top$ yields the equations of motion in modal space:

$$\left[-\mathbf{\Phi}^\top(\mathbf{M} + \mathbf{A})\mathbf{\Phi}\omega^2 + \mathrm{i}\mathbf{\Phi}^\top\mathbf{B}\mathbf{\Phi}\omega + \mathbf{\Phi}^\top\mathbf{C}\mathbf{\Phi}\right]\overline{\boldsymbol{\xi}} = \overline{\mathbf{F}}, \tag{16}$$

$$\left[-(\overline{\mathbf{M}} + \overline{\mathbf{A}})\omega^2 + \mathrm{i}\overline{\mathbf{B}}\omega + \overline{\mathbf{C}}\right]\overline{\boldsymbol{\xi}} = \overline{\mathbf{F}}, \tag{17}$$

where overbars denote variables in the modal space, e.g., $\overline{\mathbf{M}} = \mathbf{\Phi}^\top\mathbf{M}\mathbf{\Phi}$, etc. Power spectral densities in modal space follow by applying the same transformations to S_ξ and S_F.

TABLE 2: Comparison of equilibrium position of the system for the individual FOWT with wind load.

DOF	MoorPy [m]	SIMA [m]	Difference [%]
FOWT (x)	19.27	19.18	0.45
FOWT (y)	19.27	19.34	0.36

TABLE 3: Comparison of equilibrium positions of system for the 2 × 2 FOWTs with shared moorings with wind load.

DOF	MoorPy [m]	SIMA [m]	Difference [%]
FOWT 1 (x)	39.51	39.07	1.13
FOWT 1 (y)	38.60	37.80	2.12
FOWT 2 (x)	1655.12	1654.00	0.07
FOWT 2 (y)	40.37	39.52	2.15
FOWT 3 (x)	37.92	37.61	0.82
FOWT 3 (y)	-1576.83	-1577.00	0.01
FOWT 4 (x)	1653.35	1653.00	0.02
FOWT 4 (y)	-1575.24	-1576.00	0.05

3.3. Time-Domain Simulation

For the time-domain analysis of both the single and 4 FOWT setups, a SIMA [4] solver coupling SIMO [24] and RIFLEX [25] is used. SIMO simulates the rigid body (spar buoys) and RIFLEX simulates the mooring lines using the finite element method (FEM). Damping from the mooring lines is considered for comparison with the frequency-domain results.

The hydrostatic and hydrodynamic information about the spar buoy obtained from HydroD, such as the hydrostatic stiffness, first-order motion transfer function, radiation data (added mass and wave-radiation damping) and full QTFs for second-order difference-frequency wave forces, are imported into SIMA. For this case, irregular waves described by the JONSWAP spectrum are used with the significant wave height $H_s = 7$ m and the peak period $T_p = 10$ s with waves coming in at 45°. Following [22], the JONSWAP spectrum is formulated as a modification of the Pierson-Moskowitz wave spectrum:

$$S(\omega) = A_\gamma S_{\text{PM}}(\omega)\gamma^{\exp\left(-0.5\left(\frac{\omega-\omega_p}{\sigma\omega_p}\right)^2\right)}, \tag{18}$$

where $\gamma = 3.3$ is the non-dimensional peak shape parameter, $\sigma = \sigma_a$ for $\omega \le \omega_p$ and $\sigma = \sigma_b$ for $\omega > \omega_p$ is the spectral width parameter, and $A_\gamma = 0.2/(0.065\gamma^{0.803} + 0.125)$ is a normalizing factor (for $\sigma_a = 0.07$ and $\sigma_b = 0.09$). The Pierson-Moskowitz (PM) wave spectrum $S_{\text{PM}}(\omega)$ is given by

$$S_{\text{PM}}(\omega) = \frac{5}{16}H_s^2\omega_p^4\omega^{-5}\exp\left(-\frac{5}{4}\left(\frac{\omega}{\omega_p}\right)^{-4}\right), \tag{19}$$

in which $\omega_p = 2\pi/T_p$ is the angular spectral peak frequency.

To verify the initial conditions prior to wave excitation, the wind-loaded equilibrium positions from SIMA are compared against the solutions from MoorPy. The differences are reported in Table 2 (single FOWT) and Table 3 (four FOWTs with shared moorings). The agreement is close, with maximum discrepancies of about 2 %.

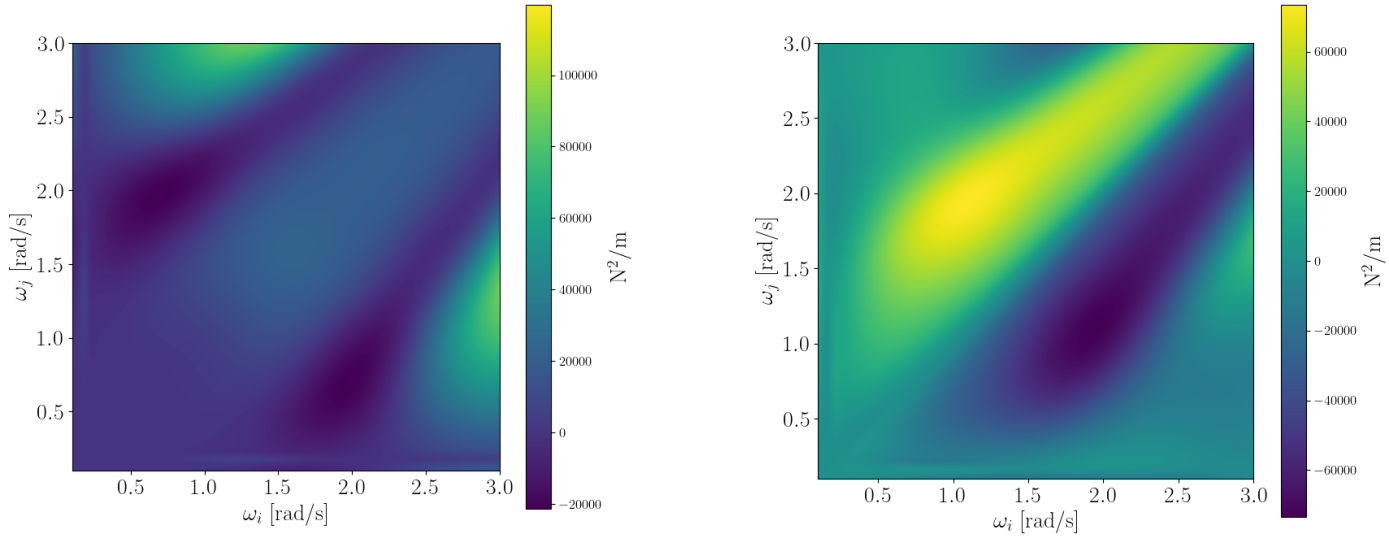

(a) Real part **(b) Imaginary part**

FIGURE 5: Full quadratic transfer function (QTF).

4. RESULTS

4.1. Mode Shapes and Natural Frequencies

Fig. 6 shows the obtained mode shapes and natural periods of the 4-unit farm with shared mooring system, following the procedure described in Section 3.2. Red dots mark the FOWTs, gray lines are mooring lines, and blue arrows indicate the modal displacement direction at each FOWT. There are two distinct types of mode shapes:

1. Odd mode shapes that align with the direction of the wind load.

2. Even mode shapes that are orthogonal to the direction of the wind load.

For the shared-mooring array, the natural periods cluster into two bands: 112.46 s to 114.66 s for modes 1–4 (top row in Fig. 6) and 200.84 s to 213.89 s for modes 5–8 (bottom row). The individual FOWT system has two equal natural periods at 139.59 s lying in between these two bands. These long periods relative to typical wave periods indicate susceptibility to second-order (slow-drift) excitation. In subsequent sections, these eigenvectors (mode shapes) are used to conduct a modal analysis of the system. The natural frequencies obtained here are lower than those reported in [9]. The reason is that a semi-submersible FOWT was considered in [9] while the present work (and [10]) uses a spar FOWT.

4.2. Frequency-Domain Results

The standard deviation of the second-order motions, namely the square root of the zeroth spectral moment of the response PSD, is of particular interest for estimating extremes. Initial results of σ for all DOFs at the chosen sea state using Newman's approximation are listed in Table 4. The values here are relatively small. The results are sensitive to the sea state parameters (H_s and T_p) and to the drag coefficient C_d. Applying the stochastic linearization of drag in Sec. 3.1, the drag coefficient converged to $C_d \approx 0.2$, which reduces damping and increases σ by about 70 % relative to the initial $C_d = 1.0$ guess. Unless stated otherwise, results are reported with $C_d = 0.2$. For the single-turbine baseline (not shown in the table), the surge and sway standard deviations are 0.867 m, smaller than those of the shared-mooring array.

TABLE 4: Standard deviations of low-frequency surge and sway motions (m) for the 2 × 2 FOWTs with shared moorings at H_s = 7.0 m, T_p = 10 s.

DOF	Newman's approximation		Full QTF	SIMA
	$C_d = 1.0$	$C_d = 0.2$	$C_d = 0.2$	$C_d = 0.2$
Surge FOWT 1	0.577	0.987	1.057	1.057
Sway FOWT 1	0.582	0.995	1.058	1.058
Surge FOWT 2	0.596	1.020	1.077	1.077
Sway FOWT 2	0.596	1.020	1.077	1.077
Surge FOWT 3	0.566	0.968	1.042	1.042
Sway FOWT 3	0.566	0.968	1.042	1.042
Surge FOWT 4	0.582	0.995	1.058	1.058
Sway FOWT 4	0.577	0.987	1.057	1.057

Fig. 7 shows the amplitude of the slowly varying forces F_{SV}. The oscillation pattern of F_{SV} varies for each FOWT. FOWTs 1 and 4 display longer-period oscillations, whereas FOWTs 2 and 3 exhibit shorter-period oscillations that attenuate as μ approaches 0.35 rad/s. As expected, F_{SV} depends on wave heading and turbine position within the array, consistent with [9].

The surge and sway frequency responses in Fig. 8 show multiple peaks near the natural frequencies (see values on the top of sub figures in Fig. 6). This occurrence arises from the contribution of each FOWT response to various modes in Fig. 6, each with distinct intensities. FOWT 2 exhibits the highest response. This heightened response can be attributed to the slack mooring

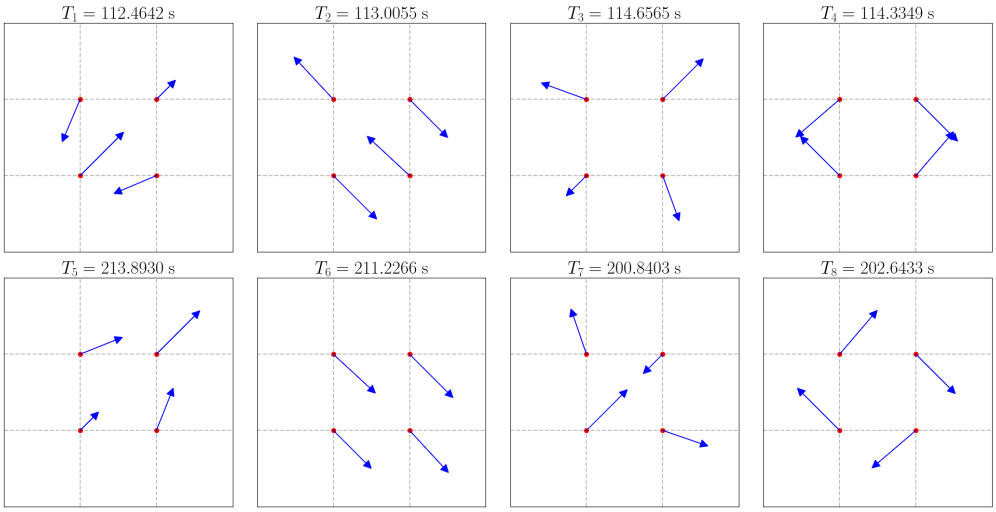

FIGURE 6: Eigenmode shapes with wind loads.

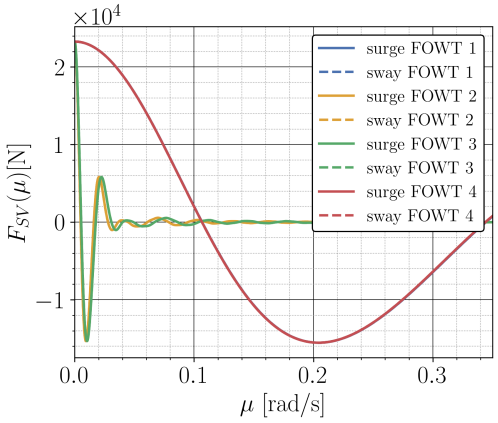

FIGURE 7: Amplitudes of the slowly varying forces.

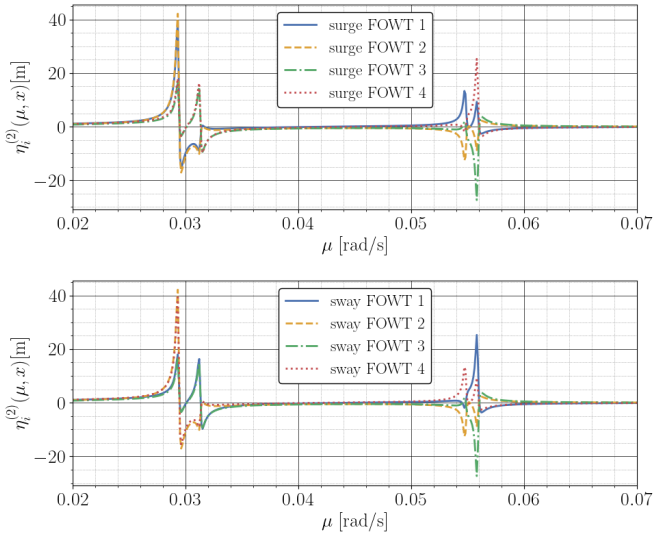

FIGURE 8: Nodal responses for H_s = 7.0 m and T_p = 10 s in surge and sway.

lines attached to FOWT 2 due to a 45° wind forcing application. Here, shared lines maintain uniform tension, resulting in reduced resistance to motion for FOWT 2, in agreement with [8]. The response PSDs in Fig. 9 mirror these features, with peaks aligned to the natural frequencies. FOWT 2 again shows the highest peaks in both surge and sway.

The modal response spectrum is shown in Fig. 10 with a logarithmic y-axis. The peaks of the response spectra occur close to the natural frequency of the corresponding modes. The response is relatively low at large difference frequencies even though the QTF for difference-frequency excitation force is larger at this region. The shared mooring system only has a significant response at higher periods/lower frequencies. Moreover, the odd modes $(1, 3, 5, 7)$ exhibit a significantly higher response than the even modes $(2, 4, 6, 8)$. This pattern is also evident in the modal excitation-load spectrum depicted in Fig. 11. The odd mode shapes are considerably more prevalent and thus more important than the even modes.

Newman's approximation is accurate at small difference frequencies, but its accuracy degrades as the difference frequencies increase. Fig. 12 compares Newman's approximation with full QTF at the maximum difference frequency, $\mu_{\max} = 0.35\,\text{rad/s}$. Newman's approximation and full QTF differ but are relatively close at lower frequencies. As expected, there is a substantial amount of difference in the imaginary component of the QTF. Newman's approximation assumes that the imaginary part of QTF is always zero, while the full QTF predicts nonzero values as long as the difference frequency μ is not zero. For $\mu_{\max} = 0.35\,\text{rad/s}$, it is evident that the imaginary part of the QTF is considerably greater than the real part. This is a signal that larger errors may occur if Newman's approximation is adopted to estimate the slow-drift excitation loads at this difference frequency.

To assess the impact of this underestimation, the same analysis was conducted but using full QTF. This approach requires significantly more computational time. While Newman's approximation took only 1 minute, the full QTF method took nearly 20

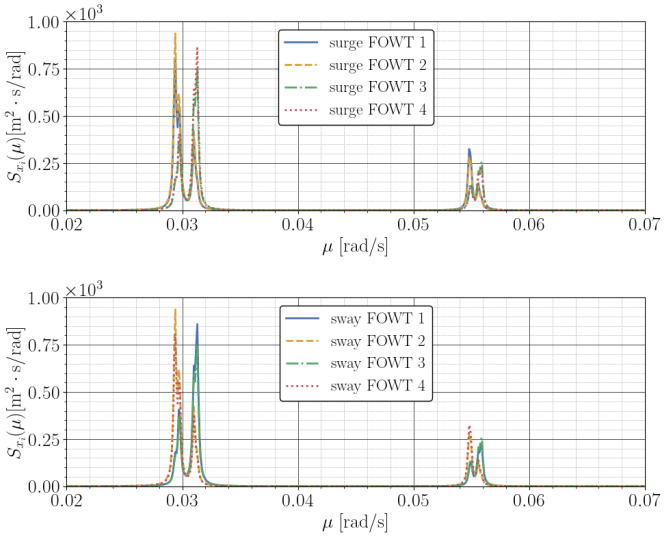

FIGURE 9: Power spectral densities (PSDs) of surge and sway for H_s = 7.0 m and T_p = 10 s using Newman's approximation.

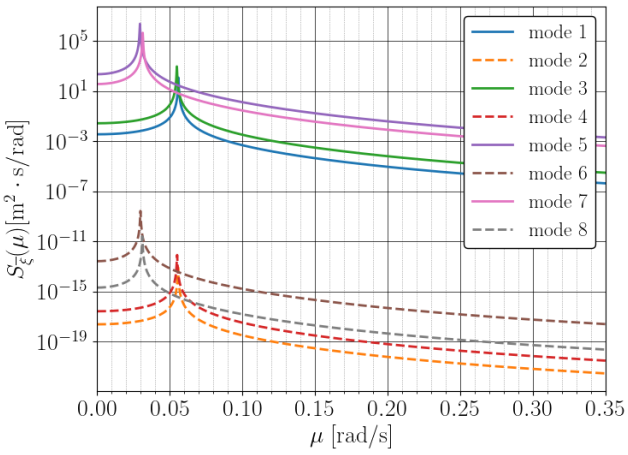

FIGURE 10: Modal response spectra for H_s = 7.0 m and T_p = 10 s using Newman's approximation.

minutes. Standard deviations σ for all DOFs obtained with full QTF are listed in Table 4. Newman's approximation underestimates σ relative to the full QTF results.

As shown in Fig. 13, the behavior of the slowly varying force amplitudes in the full QTF is much different from Newman's approximation due to the phase of the full QTF interaction with the exponent oscillatory term. Consistently, the force power spectral density $S_F(\mu)$ is significantly higher with the full QTF at moderate-to-high difference frequency (μ). See the comparison in Fig. 14.

Comparing the surge and sway response PSDs based on full QTF (Fig. 15) with those from Newman's approximation (Fig. 9) shows that peaks are lower in the lower natural-frequency band (0.02 rad s^{-1} to 0.04 rad s^{-1}) but higher in the upper band (0.04 rad s^{-1} to 0.06 rad s^{-1}) when full QTF is used. This result can be attributed to the effective damping coefficient. As shown

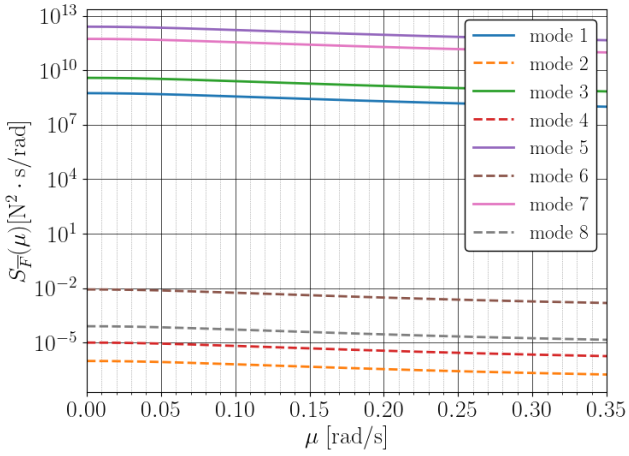

FIGURE 11: Mode excitation-load spectra for H_s = 7.0 m and T_p = 10 s using Newman's approximation.

before, σ_{u_r} for the full QTF method is higher since the damping coefficient is proportional to the damping of the system increases as well.

At low frequencies, S_F from both full QTF and Newman's approximation is relatively close, leading to broader but lower peaks. As the frequency increases, $S_F(\mu)$ from full QTF can exceed Newman's by more than a factor of two, so the corresponding response peaks remain higher despite the increased damping. In short, Newman's approximation tends to overpredict the response near the lowest natural frequencies and underpredict it at higher difference frequencies. These trends underscore the need to validate the stochastic linearization of damping and the use of Newman's approximation against model tests when accuracy at moderate or large μ is required.

Frequency domain analysis revealed the presence of multiple peaks in the nodal response of the shared mooring system in contrast to the individual mooring system which only has one peak at one natural frequency. This shows that each FOWT contributes to multiple mode shapes at their natural periods, thus exhibiting a different dynamic behavior as compared to the individual mooring system.

Frequency analysis in the modal domain showed that modes that excite in alignment with the wind forcing (odd modes) have higher modal excitation-loads and are thus more important than the orthogonal modes (even modes). Specifically, of the odd modes, mode 5 and mode 7 have the higher modal response and modal excitation-loads than mode 1 and mode 3. Among them, mode 1 and 3 are more likely to cause failure in shared lines while mode 5 and 7 are more likely to cause failure in anchor lines.

4.3. Time-Domain Results

Time-domain results corroborate the multiple-peak structure seen in the frequency-domain analysis (Fig. 16). After updating the added mass by 7 %, the slow-drift natural periods agree closely, shifts of 6 s for FOWT 1 (sway), FOWT 3 (surge and sway), and FOWT 4 (surge), corresponding to a maximum error of about 2.6 %; the remaining DOFs show shifts of 2 s (about 1 %). This indicates that the SIMA model is slightly stiffer than

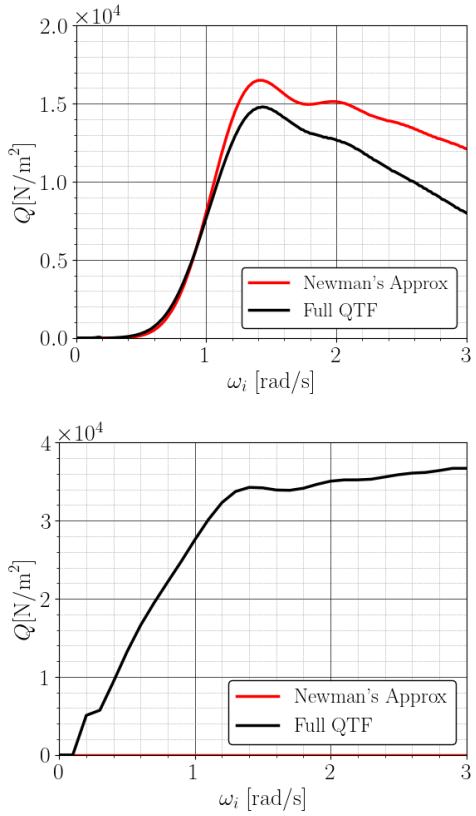

FIGURE 12: Comparison of full QTF and Newman's approximation for the real (top) and imaginary (bottom) components at μ = 0.35 rad/s.

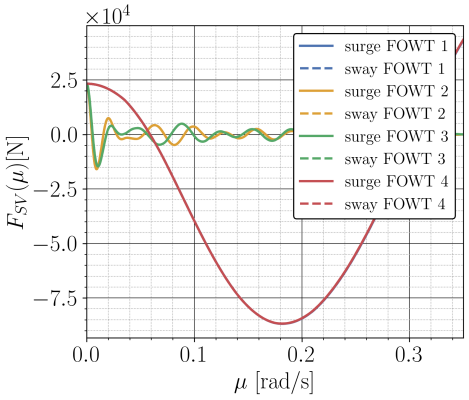

FIGURE 13: Amplitudes of slowly varying forces.

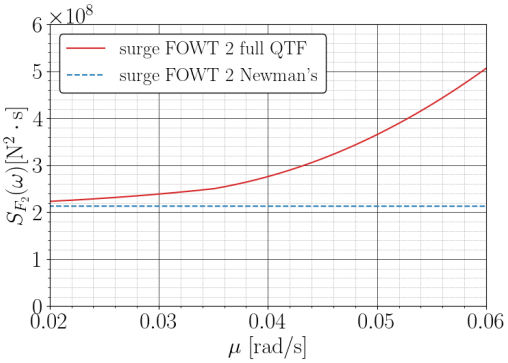

FIGURE 14: Comparison of force PSD for FOWT 2 in surge between full QTF and Newman's approximation.

the frequency-domain model. It might be explained by the fact that the frequency-domain model uses the mooring restoring matrix calculated at the equilibrium position, while the time-domain simulations, with the mooring system modeled by a nonlinear finite element method, have a more accurate representation of the nonlinear restoring load by the mooring system.

Peak comparisons show good agreement for FOWT 1 surge, FOWT 2 surge and sway, and FOWT 4 sway; for the other DOFs, the frequency-domain solution overpredicts the PSD. The corresponding standard deviations are listed in Table 4. Consistent with the PSDs, the time-domain σ values match the frequency-domain results closely for FOWT 1 surge, FOWT 2 surge and sway, and FOWT 4 sway (maximum error 3.7 %); for the remaining DOFs, errors are up to 19 %.

The time-domain PSDs also exhibit multiple low-frequency peaks, consistent with the frequency-domain findings. Small differences in peak ordinates likely reflect the narrow-banded nature of the response and its sensitivity to simulation duration.

The PSD curves in Fig. 16 were obtained using a standard FFT of the time-series data. Because the longest natural period exceeds 200 s, the duration of the time-domain simulation (T_d) must be sufficiently long to provide adequate frequency resolution. The lowest resolvable non-zero frequency is $f_{\min} = 1/T_d$. In this study, T_d was chosen to ensure that the peak values in the PSD curves of Fig. 16 are accurately resolved; an overly short simulation would otherwise smear these sharp peaks. Similarly, the PSD curves obtained from the frequency-domain approach require a sufficiently fine resolution in the difference frequency, μ. When performing a full QTF analysis, the hydrodynamic computations must therefore use a frequency grid such that the minimum difference frequency is much smaller than the relevant natural frequencies. This requirement has entailed a significantly large computational effort in computing the full QTF matrix.

5. CONCLUSIONS

Modal, frequency-domain, and time-domain analyses were performed for a 2×2 shared-mooring lattice and compared with an individually moored baseline to characterize low-frequency dynamics and line-tension behavior. The main findings are:

1. Nodal and modal analyses show that the shared-mooring array exhibits multiple LF peaks associated with distinct eigenfrequencies and mode shapes, whereas the individually moored single-turbine baseline displays a single narrow peak near its natural frequency. Time-domain simulations in SIMA (coupled SIMO–RIFLEX) agree closely with frequency-domain predictions and corroborate these observations.

2. In frequency-domain analysis, the computed response is highly sensitive to the drag coefficient because damping is incorporated through stochastic linearization. To avoid ad

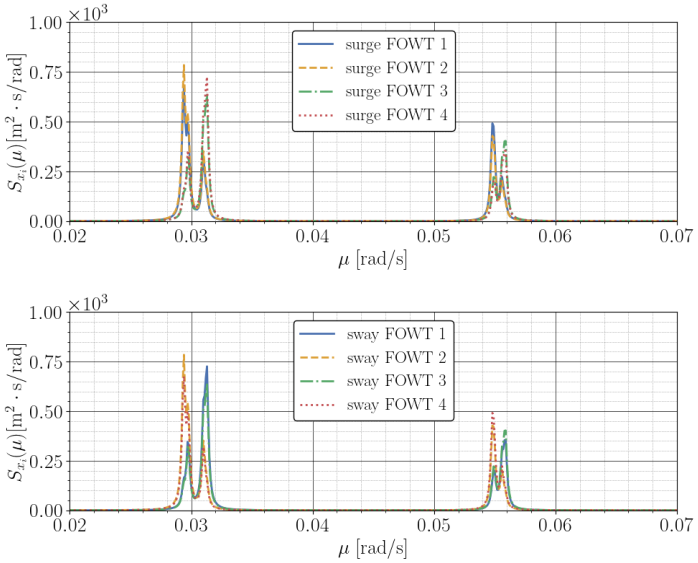

FIGURE 15: Power spectral densities of response for H_s = 7.0 m and T_p = 10 s using full QTF in surge and sway.

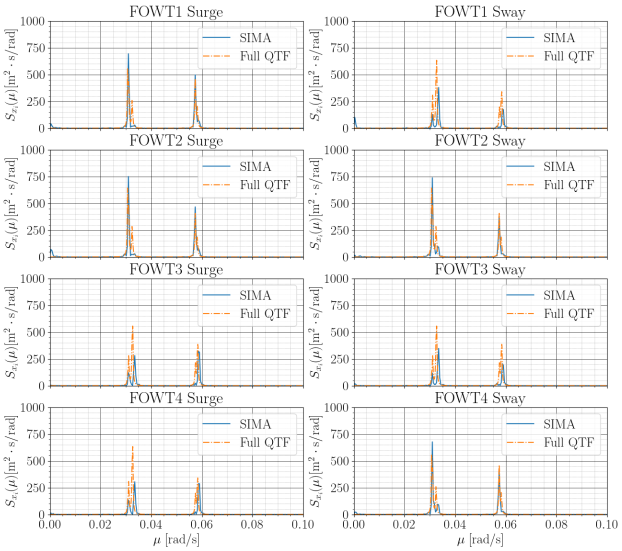

FIGURE 16: Comparison of PSDs between SIMA and frequency domain results for the shared mooring system.

hoc parameter selection, a stochastic-linearization framework is adopted that automatically determines the drag coefficient from predefined, KC-dependent correlations and evaluates the resulting linearized damping.

3. Comparison between Newman's approximation and the full-QTF approach shows that Newman's approximation typically underestimates slow-drift loads and implies lower effective damping: this combination can over-predict response near the lowest natural frequencies while underpredicting response at higher difference frequencies.

These results reinforce that shared-mooring arrays of FOWTs exhibit different dynamic behavior from individually moored turbines, motivating further studies on array-level modal dynamics, slowly-varying loads and motions, and robust design and analysis for FOWT farms employing shared mooring systems.

ACKNOWLEDGMENTS

This work was carried out at Technical University of Denmark as part of the first author's MSc thesis. The first author gratefully acknowledges DNV Digital Solutions for providing access to the Sesam software package during his thesis work. The second and third authors acknowledge the support from EU's CETPartnership (CETP-2023-00145) and Innovation Fund Denmark (3170-00020B) for their writing time on this paper through the ESOMOOR project (www.esomoor.eu). The views and opinions expressed are those of the author(s) only and do not necessarily reflect those of the European Union or the CETPartnership. Neither the European Union nor the granting authority can be held responsible for them.

REFERENCES

[1] Civier, Laure, Chevillotte, Yoan, Bles, Guilhem, Damblans, Guillaume, Montel, Frédéric, Davies, Peter and Marco, Yann. "Visco-elasto-plastic characterization and modeling of a wet polyamide laid-strand sub-rope for floating offshore wind turbine moorings." *Ocean Engineering* Vol. 303 (2024): p. 117722. DOI 10.1016/j.oceaneng.2024.117722.

[2] Liang, Guodong, Merz, Karl and Jiang, Zhiyu. "Modeling of a Shared Mooring System for a Dual-Spar Configuration." *Volume 9: Ocean Renewable Energy*. 2020. American Society of Mechanical Engineers. DOI 10.1115/omae2020-18467.

[3] Irvine, H. Max. *Cable structures*, unabridged republication ed. Constable, London (1992). Literaturangaben.

[4] SINTEF Ocean. "SIMA." URL https://www.sintef.no/en/software/sima/.

[5] Connolly, Patrick and Hall, Matthew. "Comparison of pilot-scale floating offshore wind farms with shared moorings." *Ocean Engineering* Vol. 171 (2019): pp. 172–180. DOI 10.1016/j.oceaneng.2018.08.040.

[6] Larsen, Torben Juul and Hansen, Anders Melchior. *How 2 HAWC2, the user's manual*. Risø, Risø National Laboratory, Roskilde (2020).

[7] Gözcü, Ozan, Kontos, Stavros and Bredmose, Henrik. "Dynamics of two floating wind turbines with shared anchor and mooring lines." *Journal of Physics: Conference Series* Vol. 2265 No. 4 (2022): p. 042026. DOI 10.1088/1742-6596/2265/4/042026.

[8] Goldschmidt, Marek and Muskulus, Michael. "Coupled Mooring Systems for Floating Wind Farms." *Energy Procedia* Vol. 80 (2015): pp. 255–262. DOI 10.1016/j.egypro.2015.11.429.

[9] Sauder, Thomas. "Second-order wave loads on floating wind parks with shared mooring." *Journal of Physics:*

Conference Series Vol. 2626 No. 1 (2023): p. 012038. DOI 10.1088/1742-6596/2626/1/012038.

[10] Hall, Matthew, Housner, Stein, Lozon, Ericka and Sirnivas, Senu. "Shared Mooring Systems for Deep-Water Floating Wind Farms." Technical report no. National RenewableEnergy Laboratory, Golden, Colorado. 2021.

[11] Lozon, Ericka and Hall, Matthew. "Coupled loads analysis of a novel shared-mooring floating wind farm." *Applied Energy* Vol. 332 (2023): p. 120513. DOI 10.1016/j.apenergy.2022.120513.

[12] Silva de Souza, Carlos Eduardo, Berthelsen, Petter Andreas, Eliassen, Lene, Bachynski, Erin Elizabeth, Engebretsen, Espen and Haslum, Herbjørn. *Definition of the INO WINDMOOR 12 MW base case floating wind turbine*. SINTEF Ocean AS (2021). URL https://hdl.handle.net/11250/2723188.

[13] Jonkman, Bonnie, Mudafort, Rafael M, Platt, Andy, E. Branlard, Sprague, Mike, Ross, Hannah, Jjonkman, HaymanConsulting, Hall, Matt, Slaughter, Derek, Vijayakumar, Ganesh, Buhl, Marshall, Russell9798, Bortolotti, Pietro, Reos-Rcrozier, Shreyas Ananthan, Michael, S., Rood, Jon, Rdamiani, Nrmendoza, Sinolonghai, Pschuenemann, Ashesh2512, Kshaler, Housner, Stein, Psakievich, Bendl, Kurt, Carmo, Lucas, Quon, Eliot and Mattrphillips. "OpenFAST/openfast: v3.5.0." (2023). DOI 10.5281/ZENODO.7942867.

[14] Jonkman, Jason and Shaler, Kelsey. "FAST.Farm User's Guide and Theory Manual." URL https://www.nrel.gov/docs/fy21osti/78485.pdf.

[15] Hall, Matthew. "MoorDyn V2: New Capabilities in Mooring System Components and Load Cases." *Volume 9: Ocean Renewable Energy*. 2020. American Society of Mechanical Engineers. DOI 10.1115/omae2020-19341.

[16] Hall, Matthew and Connolly, Patrick. "Coupled Dynamics Modelling of a Floating Wind Farm With Shared Mooring Lines." *Volume 10: Ocean Renewable Energy*. 2018. American Society of Mechanical Engineers. DOI 10.1115/omae2018-78489.

[17] Bak, Christian, Zahle, Frederik, Bitsche, Robert, Kim, Taeseong, Yde, Anders, Henriksen, {Lars Christian}, Hansen, {Morten Hartvig}, Blasques, {José Pedro Albergaria Amaral}, Gaunaa, Mac and Natarajan, Anand. "The DTU 10-MW Reference Wind Turbine." (2013). Danish Wind Power Research 2013 ; Conference date: 27-05-2013 Through 28-05-2013.

[18] Hall, Matthew, Housner, Stein, Sirnivas, Senu and Wilson, Samuel. "MoorPy (Quasi-Static Mooring Analysis in Python)." (2021). DOI 10.11578/dc.20210726.1. URL https://www.osti.gov/biblio/code-61138.

[19] Orcina Ltd. "OrcaFlex." URL https://www.orcina.com.

[20] DNV. "HydroD." URL https://www.dnv.com/services/hydrodynamic-analysis-and-stability-analysis-software-hydrod-14492/.

[21] Shao, Yan-Lin, You, Jikun and Glomnes, Einar Bernt. "Stochastic Linearization and its Application in Motion Analysis of Cylindrical Floating Structure With Bilge Boxes." *Proceedings of the ASME 2016 35th International Conference on Ocean, Offshore and Arctic Engineering*: p. V001T01A016. 2016. DOI 10.1115/OMAE2016-55059.

[22] DNV. "DNV-RP-C205 Environmental conditions and environmental loads." (2025). Edition 2025-04.

[23] DNV. "Sesam Package Description." (2024). URL https://mysoftware.dnv.com/knowledge-centre/sesam/. Software suite for hydrodynamic and structural analysis of offshore wind, offshore oil and gas, and maritimestructures.

[24] DNV. "SIMO." URL https://www.dnv.com/services/complex-multibody-calculations-simo-2311/.

[25] DNV. "RIFLEX." URL https://www.dnv.com/services/riser-analysis-software-for-marine-riser-systems-riflex-2312/.